Journal of
Marine Science and Engineering

MDPI

Article

Non-Equilibrium Scour Evolution around an Emerged Structure Exposed to a Transient Wave

Deniz Velioglu Sogut [1,*], Erdinc Sogut [2], Ali Farhadzadeh [3] and Tian-Jian Hsu [4]

[1] Department of Ocean Engineering and Marine Sciences, College of Engineering and Science, Florida Institute of Technology, Melbourne, FL 32901, USA
[2] Department of Geology and Geophysics, Woods Hole Oceanographic Institution, Falmouth, MA 02543, USA; erdinc.sogut@whoi.edu
[3] Department of Civil Engineering, College of Engineering and Applied Sciences, Stony Brook University, Stony Brook, NY 11794, USA; ali.farhadzadeh@stonybrook.edu
[4] Department of Civil and Environmental Engineering, Center for Applied Coastal Research, University of Delaware, Newark, DE 19716, USA; thsu@udel.edu
* Correspondence: dvelioglusogut@fit.edu

Abstract: The present study evaluates the performance of two numerical approaches in estimating non-equilibrium scour patterns around a non-slender square structure subjected to a transient wave, by comparing numerical findings with experimental data. This study also investigates the impact of the structure's positioning on bed evolution, analyzing configurations where the structure is either attached to the sidewall or positioned at the centerline of the wave flume. The first numerical method treats sediment particles as a distinct continuum phase, directly solving the continuity and momentum equations for both sediment and fluid phases. The second method estimates sediment transport using the quadratic law of bottom shear stress, yielding robust predictions of bed evolution through meticulous calibration and validation. The findings reveal that both methods underestimate vortex-induced near-bed vertical velocities. Deposits formed along vortex trajectories are overestimated by the first method, while the second method satisfactorily predicts the bed evolution beneath these paths. Scour holes caused by wave impingement tend to backfill as the flow intensity diminishes. The second method cannot sufficiently capture this backfilling, whereas the first method adequately reflects the phenomenon. Overall, this study highlights significant variations in the predictive capabilities of both methods in regard to the evolution of non-equilibrium scour at low Keulegan–Carpenter numbers.

Keywords: Keulegan–Carpenter number; solitary wave; non slender; wave–structure interaction; FLOW-3D; SedWaveFoam

Citation: Velioglu Sogut, D.; Sogut, E.; Farhadzadeh, A.; Hsu, T.-J. Non-Equilibrium Scour Evolution around an Emerged Structure Exposed to a Transient Wave. *J. Mar. Sci. Eng.* **2024**, *12*, 946. https://doi.org/10.3390/jmse12060946

Academic Editor: Constantine Michailides

Received: 25 April 2024
Revised: 28 May 2024
Accepted: 1 June 2024
Published: 5 June 2024

1. Introduction

The increase in the magnitude and frequency of storms is a crucial aspect of climate change, where larger ocean waves lead to more frequent and harsher storm surge and flooding events. The most recent examples are Hurricanes Ian and Nicole, which made landfall in Florida on 28 September 2022 and 10 November 2022 as powerful Category 4 and 1 storms, respectively. Ian came ashore as one of the strongest storms ever to strike Florida, leaving behind massive coastal damage and widespread power outages. Nicole was the first storm to make landfall on Florida's east coast since 2005, crossing the same area that had been devastated by Ian six weeks earlier. Its massive size caused widespread heavy rainfall and high winds across the Bahamas, Florida, and the Greater Antilles, leading to power outages, substantial damage to infrastructure and residential buildings, and extensive beach erosion along Florida's east coast. These extreme flooding events underscore the need for more in-depth studies on the failures of beachfront structures in

the low-elevation urbanized coastal zones. An important factor that contributes to the failure of beachfront structures during such events is the scouring process [1,2].

Wave- and/or current-induced equilibrium scour around slender cylindrical structures has been extensively studied [3–20] due to its relevance to a wide range of applications such as offshore wind farms in the renewable energy industry and bridges in the transportation sector. Studies on the equilibrium scour of slender square structures under different flow conditions have also been conducted [17,21–23]. However, knowledge on wave-induced non-equilibrium scour processes around non-slender structures remains limited due to lack of conclusive data. Non-equilibrium scour is a constantly evolving scour pattern, as erosion and accretion are not in equilibrium. Various factors contribute to non-equilibrium scour, including changes in flow velocity, sediment size distribution, and turbulence intensity. It is commonly observed during transient flow conditions such as waves, storm-driven floods, or tidal fluctuations. Understanding non-equilibrium scour is essential for the design and maintenance of infrastructure, as it can lead to significant alterations in the bathymetry around structures, posing risks to their stability and safety. Therefore, investigating and predicting non-equilibrium scour processes is crucial for risk mitigation and the integrity of coastal and hydraulic structures. Recent field investigations have shown that wave-induced scour around beachfront structures is highly dependent on the structure's size and placement within an array [24–26]. Although these investigations provide insight into the scouring process during extreme overland flooding events, they do not contribute significantly to the accurate prediction of non-equilibrium scour around beachfront structures.

Sediment transport processes can be numerically described by an equation set that simulates the spatial and temporal evolution of a fluid flow carrying sediment as it interacts with the adjacent mobile bed [27]. Numerical models that simulate sediment transport aim to predict the overall mass flux and sediment concentration at each point in the domain with reasonable accuracy. However, the literature review shows that studies investigating the capability of these models in predicting non-equilibrium scour around non-slender structures are still lacking. This gap in knowledge motivates the current work.

The present study aims to investigate the morphological changes in a sandy bed when a transient wave interacts with an emerged non-slender square structure, using a combination of wave flume experiments and high-fidelity numerical simulations. Additionally, the effect of structure position on bed evolution was examined by considering two different layouts, one where the structure was attached to the sidewall and the other where it was positioned at the centerline. To numerically study the test cases mentioned above, two different approaches were employed.

The first approach utilized SedWaveFoam, a numerical tool that considers the sediment layer as a separate phase in addition to air and water phases and solves Reynolds-averaged Navier–Stokes (RANS) equations. This tool differs from single-phase models that rely on assumptions of bed/suspended load and bed shear stress [28–30] because it directly solves the continuity and momentum equations for sediment, water, and air phases [31]. The second approach employed FLOW-3D, which estimates sediment transport using the quadratic law of bottom shear stress for three-dimensional (3D) turbulent flow and resolves the flow field using the RANS equations. However, the morphodynamics module of FLOW-3D is case specific and requires calibration and validation to obtain robust estimations of bed evolution [32,33].

In this study, a comprehensive comparative analysis was performed to assess the predictive capabilities of the two different approaches as well as some of their shortcomings in estimating the non-equilibrium scour around a non-slender emerged square structure exposed a transient wave. It should be noted that the current version of SedWaveFoam only supports the $k - \varepsilon$ turbulence scheme, whereas FLOW-3D adopts the large eddy simulation (LES) scheme to simulate the turbulent flow characteristics. Here, the authors regard the two approaches as different tools, with discussions centered on a broad framework. The capability of the models was tested for a low Keulegan–Carpenter (KC) number, and

discussions were based on the non-equilibrium scour characteristics, suspended sediment concentration, and patterns of sediment deposits in the vicinity of the structure. The present study advances knowledge in the field of coastal and hydraulic engineering, offering guidance for scientific community on selecting the most appropriate modeling approach for similar scenarios. Overall, the effort provides valuable insights that can enhance coastal resilience in the face of dynamic environmental conditions.

This research builds on the authors' previous work [34–36], which focused on the formation and evolution of non-equilibrium scour around square non-slender vertical structures under solitary wave and/or combined flow (wave and current) actions. The authors extend their previous work by providing high-fidelity numerical investigations using a finer mesh and two different layouts to further investigate the underlying physics of the phenomenon.

2. Physical Modeling

The experiments were carried out using the 25 m long × 1.5 m wide × 1.5 m deep wave/current flume at Stony Brook University's Coastal and Hydraulic Engineering Research Laboratory (CHERL). The piston-type wet-back wavemaker had an active wave absorption system (AWAS) that minimized the effect of wave reflection. To further dampen the reflected waves, a honeycomb mesh that acted as a passive wave energy absorption system was placed at the end of the wave flume (Figure 1). A sharp-edged wooden block with cross-sectional dimensions 0.5 m × 0.5 m was placed on a 0.18 m thick sand layer with a median grain diameter of $d_{50} = 0.27$ mm. The wave paddle was programmed to generate a solitary wave as described by [37]

$$\eta(x,t) = H\,\mathrm{sech}^2(k(1-ct)) \tag{1}$$

where η is the water surface elevation, c is the wave celerity, t is time and k is the wave number defined as $\sqrt{3H/4h^3}$. The incident wave height (H) at the paddle was 10 cm, with a period (T) of 3.20 s. The wave propagated over a 0.48 m water depth (h), which was reduced to 0.30 m on the sandy bed. The flume experiments were conducted for two layouts: (1) structure attached to the sidewall (side) and (2) structure positioned at the centerline (center). The KC number used in the experiments is 3.14. While the experiments were not specifically tailored to replicate a precise real-life condition, the structure and flow parameters followed the Froude similitude with a λ = 1:40 length scale [17].

In small-scale flume experiments utilizing relatively large structures, blockage effects may arise, leading to an increase in flow velocity and potentially causing contraction scour. Various researchers have outlined specific geometric ratios necessary to ensure that blockage effects on scour depth are minimal [19,38,39]. The distance of the structure from a wall could impact the findings, leading to accelerated flow and changes in the wake structure. In potential flow theory, the wall effect is considered negligible when a structure is located at a distance from the wall equal to its dimension [40]. Therefore, the blockage ratio is not expected to significantly impact local hydrodynamics in the experiments.

The instantaneous free surface elevation was measured via eight Edinburgh Designs WG8USB resistive wave gauges (WG) with a sampling frequency of 128 Hz. The velocity field was captured by three Nortek Vectrino Acoustic Doppler Velocimeters (ADV) with a sampling rate of 25 Hz. The 3D velocity field was measured at one-third the still water depth $(h/3)$ above the sandy bed. The surface of the sand layer was scanned using an HR-Wallingford HRBP-1070 bed profiler system equipped with a laser probe with an accuracy of ±0.5 mm. The scanned area measured 2.5 m in length and 1.5 m in width. The limitations in the maneuverability of the probe arm assembly created a ~2 cm wide blind zone around the structure, necessitating manual measurement. The surface of the sandy bed was carefully leveled prior to each test, and the water level was allowed to settle and be free from disturbances before conducting each trial. The number and plan view of the instruments are shown in Figure 1. Further details on the experimental procedure can be found in [36].

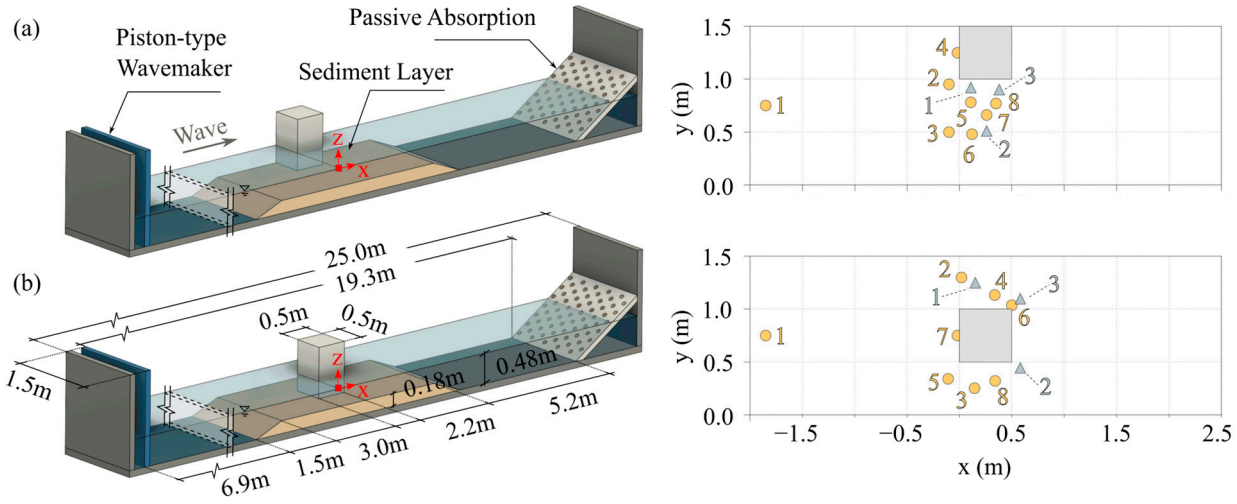

Figure 1. Experimental setup and plan view of WGs and ADVs for (**a**) side and (**b**) center layouts. Yellow circle and gray triangle represent WG and ADV, respectively.

3. Numerical Modeling

As previously mentioned, this study presents a comparative analysis of the scour formation around the structure, utilizing two high-fidelity numerical models to predict sediment motions and transport. One model employs multiphase flow physics, while the other uses conventional bedload/suspended load formulations. Here, a brief description of each model is presented.

3.1. SedWaveFoam

SedWaveFoam, developed within the OpenFOAM environment, is an open-source Eulerian two-phase model for sediment transport [31]. This model combines the SedFoam [41], InterFoam [42], and waves2Foam [43] models. The Reynolds-averaged mass conservation equations for the air (a), water (w), and sediment (s) phases [42,44] are resolved by treating the air and water as two immiscible fluids, collectively referred to as the fluid-phase (f). The sediment is modeled as a miscible phase in the fluid, resulting in a two-phase flow. To resolve the interface of the air and water phases, SedWaveFoam uses an interface tracking scheme [31,42,45]. The mass conservation equations of the fluid and sediment phases are written as follows:

$$\frac{\partial \phi^f}{\partial t} + \frac{\partial \phi^f u_i^f}{\partial x_i} = \left(\frac{\partial \phi^a}{\partial t} + \frac{\partial \phi^a u_i^a}{\partial x_i}\right) + \left(\frac{\partial \phi^w}{\partial t} + \frac{\partial \phi^w u_i^w}{\partial x_i}\right) = 0 \tag{2}$$

$$\frac{\partial \phi^s}{\partial t} + \frac{\partial \phi^s u_i^s}{\partial x_i} = 0 \tag{3}$$

where ϕ^a, ϕ^w, and ϕ^s represent the volumetric concentrations and u^a, u^w, and u^s are the velocities of the air, water, and sediment phases, respectively. The fluid-phase volumetric concentration and velocity are modelled as $\phi^f = \phi^a + \phi^w$ and $u^f = (\phi^a u^a + \phi^w u^w)/\phi^f$, respectively. The global mass conservation satisfies $\phi^a + \phi^w + \phi^s = 1$.

The simplified Reynolds-averaged momentum equations for the two-phase flow are as follows:

$$\frac{\partial \rho^f \phi^f u_i^f}{\partial t} + \frac{\partial \rho^f \phi^f u_i^f u_j^f}{\partial x_j} = -\phi^f \frac{\partial P^f}{\partial x_i} + \rho^f \phi^f g \delta_{i3} - \sigma_t \gamma_s \frac{\partial \phi^a}{\partial x_i} + \frac{\partial \tau_{ij}^f}{\partial x_j} + M_i^{fs} \tag{4}$$

$$\frac{\partial \rho^s \phi^s u_i^s}{\partial t} + \frac{\partial \rho^s \phi^s u_i^s u_j^s}{\partial x_j} = -\phi^s \frac{\partial P^f}{\partial x_i} - \frac{\partial P^s}{\partial x_i} + \rho^s \phi^s g \delta_{i3} - \sigma_t \gamma_s \frac{\partial \phi^s}{\partial x_i} + \frac{\partial \tau_{ij}^s}{\partial x_j} + M_i^{sf} \tag{5}$$

where ρ^s and ρ^f are the densities of sediment and fluid phases, and the density of the fluid phase is modelled as $\rho^f = (\phi^a\rho^a + \phi^w\rho^w)/\phi^f$. Here, the densities are adopted as $\rho^a = 1$ kg/m^3, $\rho^w = 1000$ kg/m^3, and $\rho^s = 2650$ kg/m^3. P^f and P^s stand for the fluid and particle pressures, and the fluid and particle shear stresses are symbolized by the terms τ_{ij}^f and τ_{ij}^s, respectively. g is the gravitational acceleration and δ_{i3} is the Dirac delta function. The term $\sigma_t\gamma_s$ represents the surface tension where σ_t and γ_s are the surface tension coefficient and surface curvature, respectively. The fluid stress, τ_{ij}^f is modeled using a two-equation k $-$ ε model [31,45]. The interphase momentum transfer between fluid–sediment (M_i^{fs}) and sediment–fluid (M_i^{sf}) is a function of drag force and turbulent suspension [41,46] and follows Newton's third law ($M_i^{fs} = M_i^{sf}$). The particle pressure, P^s, and particle shear stress, τ_{ij}^s, are modelled as a function of the collisional and frictional components of the intergranular interactions with the former using the kinetic theory of granular flow [47]. The reader is kindly referred to [31,41,45,46] for more detail.

3.2. FLOW-3D

FLOW-3D is a computational fluid dynamics (CFD) software package that utilizes the finite volume method (FVM) to solve the 3D Reynolds-averaged Navier–Stokes equations [48]. The model employs volume-based techniques for simulation, where the equations are formulated with area and volume porosity functions, which are essential for the Fractional Area/Volume Obstacle Representation Method, FAVOR^{TM} [49,50], while the free surface is defined using a volume of fluid (VOF) function [51]. For incompressible fluids, FLOW-3D utilizes the general mass continuity and momentum equations:

$$\frac{\partial}{\partial x_i}(u_i A_i) = 0 \tag{6}$$

$$\frac{\partial u_i}{\partial t} + \frac{1}{V_F}\left\{u_j A_j \frac{\partial u_i}{\partial x_j}\right\} = -\frac{1}{\rho}\frac{\partial P}{\partial x_i} + G_i + f_i \tag{7}$$

where $i,\ j = 1, 2, 3$ represent the 3D flow field, u_i is the fluid velocity, A_i is the fractional area open to fluid flow, t is time, V_F is the fractional volume open to flow, ρ is the fluid density, P is pressure, G_i is the body acceleration and f_i is the viscous acceleration.

The VOF function, F, satisfies the following:

$$\frac{\partial F}{\partial t} + \frac{1}{V_F}\left[\frac{\partial}{\partial x_i}(FA_i u_i)\right] = F_{DIF} \tag{8}$$

where

$$F_{DIF} = \frac{1}{V_F}\left[\frac{\partial}{\partial x_i}\left(\nu_F A_i \frac{\partial F}{\partial x_i}\right)\right] \tag{9}$$

and the diffusion coefficient is $\nu_F = \sigma_c\mu_f/\rho$. The constant, σ_c, is referred to as turbulent Schmidt number, and μ_f is the dynamic viscosity of fluid.

The turbulence models implemented in FLOW-3D differ slightly from conventional formulations due to the inclusion of the FAVOR^{TM} method in the equations and a generalized treatment of turbulence production associated with buoyancy forces [48].

Notably, FLOW-3D offers several turbulence model closures, including the two-equation k $-$ ω, renormalization group (RNG) k $-$ ε, and large eddy simulation (LES) [48,49]. Moreover, the hydrodynamic solver of FLOW-3D is fully coupled with a sediment transport module that simulates morphological changes resulting from various physical processes, such as bedload transport, entrainment, and deposition. The standard wall function is employed to evaluate bed shear stress in 3D turbulent flows, incorporating bed surface roughness proportional to the median grain size:

$$k_s = c_{\text{rough}} d_{50} \tag{10}$$

where k_s is the Nikuradse roughness of the bed surface, c_{rough} is a user-defined coefficient with default value 2.5, and d_{50} is the median grain size.

In FLOW-3D, the suspended sediment is modeled as a scalar mass concentration that is assumed to be uniform across each computational cell and coupled with the density and viscosity of the fluid cell. To simulate the entrainment of sediment grains, FLOW-3D employs the equation of [52] to calculate the lift velocity of the entrained sediment grains.

$$u_{\text{lift}} = \alpha \mathrm{n}_s d_*^{0.3} \left(\theta - \theta'_{\text{cr}}\right)^{1.5} \sqrt{\frac{\|g\| d_{50} \left(\rho_s - \rho_f\right)}{\rho_f}} \tag{11}$$

where u_{lift} is the entrainment lift velocity of sediment, α is the entrainment parameter with a recommended value of 0.018 [52], n_s is the vector normal to the bed interface, θ and θ_{cr} are the local and critical Shields parameters given by [53], $\|g\|$ is the magnitude of the gravitational acceleration, ρ_s and ρ_f are the sediment and fluid densities, respectively, and d_* is a dimensionless grain diameter given by the following equation:

$$d_* = d_{50} \left[\frac{\rho_f \left(\rho_s - \rho_f\right) \|g\|}{\mu_f^2}\right]^{1/3} \tag{12}$$

The settling velocity of a sediment grain is given as follows [53]:

$$u_{\text{settling}} = \frac{\nu_F}{d_{50}} \left[\left(10.36^2 + 1.049 d_*^3\right)^{0.5} - 10.36\right] \tag{13}$$

The bedload transport in each mesh cell can be calculated by three different formulations: Nielsen [54]

$$\Phi = \beta_{\text{Nie}} \theta^{0.5} \left(\theta - \theta'_{\text{cr}}\right) \tag{14}$$

van Rijn [55]

$$\Phi = \beta_{\text{VR}} d_*^{-0.3} \left(\frac{\theta}{\theta'_{\text{cr}}} - 1\right)^{2.1} \tag{15}$$

Meyer-Peter and Müller [56]

$$\Phi = \beta_{\text{MPM}} \left(\theta - \theta'_{\text{cr}}\right)^{1.5} \tag{16}$$

Here, Φ is the dimensionless bed-load transport rate; β_{Nie}, β_{VR}, and β_{MPM} are coefficients typically taken as 12.0, 0.053, and 8.0, respectively.

The suspended sediment concentration is calculated as follows:

$$\frac{\partial c_s}{\partial t} + \nabla \cdot (u_s c_s) = \nabla \cdot \nabla (D c_s) \tag{17}$$

where c_s is the suspended sediment volume concentration, D is the diffusivity, u_s is the suspended sediment velocity calculated as $u_s = \overline{u} + u_{\text{settling}} c_s$, $\overline{u}$ being the velocity of the fluid–sediment mixture.

3.3. Implementation

To accurately recreate the water surface variations recorded at WG1, the SedWaveFoam model requires a sufficient number of harmonics, defined by their amplitudes, phases, and periods. To generate the input boundary conditions, the incident wave signal recorded at WG1 was transformed using the fast Fourier transform (FFT) algorithm, and its harmonics were used. The rigid boundaries of the numerical wave flume (NWF) were defined as no-slip/wall boundaries. To prevent wave reflection from the landward end, an absorption boundary condition was applied at the outlet, where an inward corrective velocity was

generated to absorb the incident wave. The depth of the water, gravitational acceleration, and the free surface height of the border were factors considered in determining this velocity [57,58].

The incident wave time series measured at WG1 was directly applied at the inlet of the FLOW-3D NWF, with the flume bottom, sidewalls, and structure defined as wall/no-slip boundaries. The NWF had a wave absorbing (sponge) layer, where an artificial linear damping force was implemented to dissipate wave motion [48]. The wave-absorbing boundary was enforced by selecting an outflow boundary condition at the outlet.

The index of agreement (IA) metric [59] was employed to measure the accuracy of the simulations. IA accounts for phase disagreements, where IA = 1 and IA = 0 indicate perfect agreement and disagreement, respectively. To that end, the mesh was refined until the calculated IA for the measured versus computed horizontal velocity components, u, remained relatively unchanged (Figure 2). Mesh independence was achieved at a minimum cell size of 2.5 mm for both models. The center layout yielded the same results as the side layout.

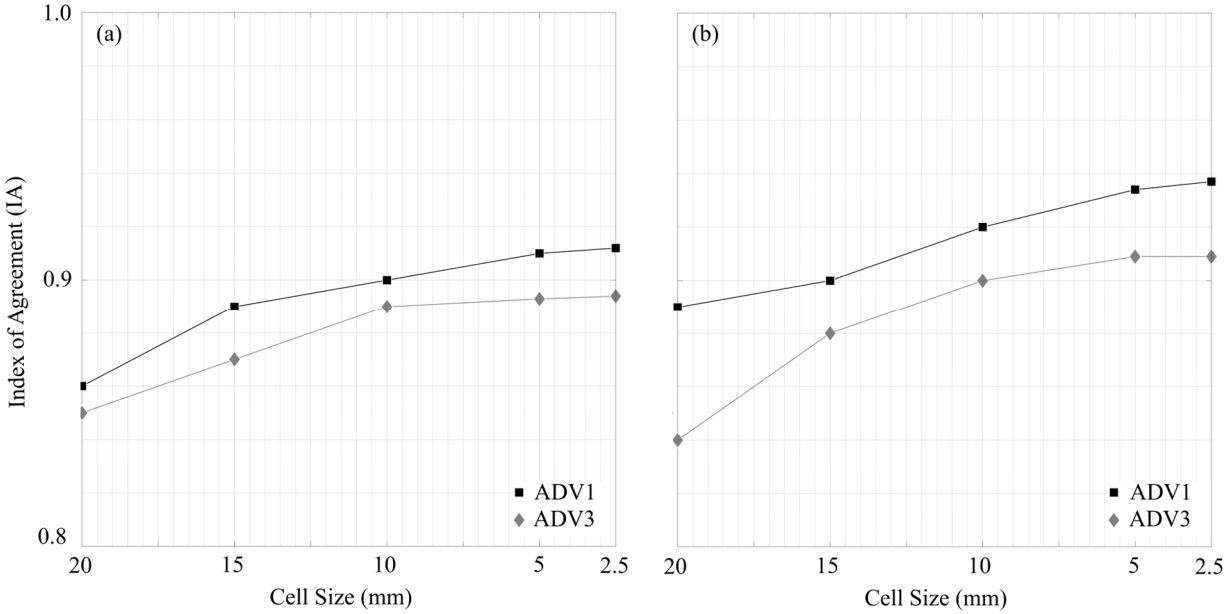

Figure 2. Grid sensitivity analyses based on the horizontal velocity component, u, captured by ADV1 and ADV3 for side layout: (**a**) SedWaveFoam; (**b**) FLOW-3D.

Figure 3 illustrates the final mesh structure utilized in the NWF. The largest cell size on the $x - y$ plane was 25 mm, which was gradually refined to a smaller cell size near the structure. The optimal cell size of 2.5 mm, as determined from grid sensitivity analyses, was employed in the refinement area marked by a dashed rectangle (Figure 3). Moreover, the region spanning from $z = -0.33$ m to $z = -0.30$ m underwent further refinement from 5 mm to 0.5 mm to achieve a more precise prediction of scouring.

To ensure model stability and convergence, the simulations used an adaptive time step with a maximum Courant number of 0.2. The model outputs had a sampling rate of 25 Hz, consistent with that of the ADVs. The total number of grid points in the FLOW-3D NWF for the side layout was ~7.2×10^6 and the clock time for a 15 s simulation was 102 h using 8 cores of a 12th Gen Intel Core i9-12900KF processor. The total number of grid points for the center layout, on the other hand, was ~17.4×10^6, with 130 h clock time. Even though the same variable mesh was adopted in both models in the vicinity of the structure, the SedWaveFoam NWF required longer wave generation and absorption zones for numerical stability. This resulted in an increase in the total number of grid points to ~22.5×10^6 and ~44.2×10^6 for the side and center layouts, respectively. The clock time of the 15 s SedWaveFoam simulation was 300 h for the side layout and 624 h for the center layout on

Blueshark High Performance Computing Cluster at Florida Tech with 10 × 2 × Hexa-Core Intel Xeon X5650 @ 2.67GHz CPUs (120 cores). (Intel, Santa Clara, CA, USA).

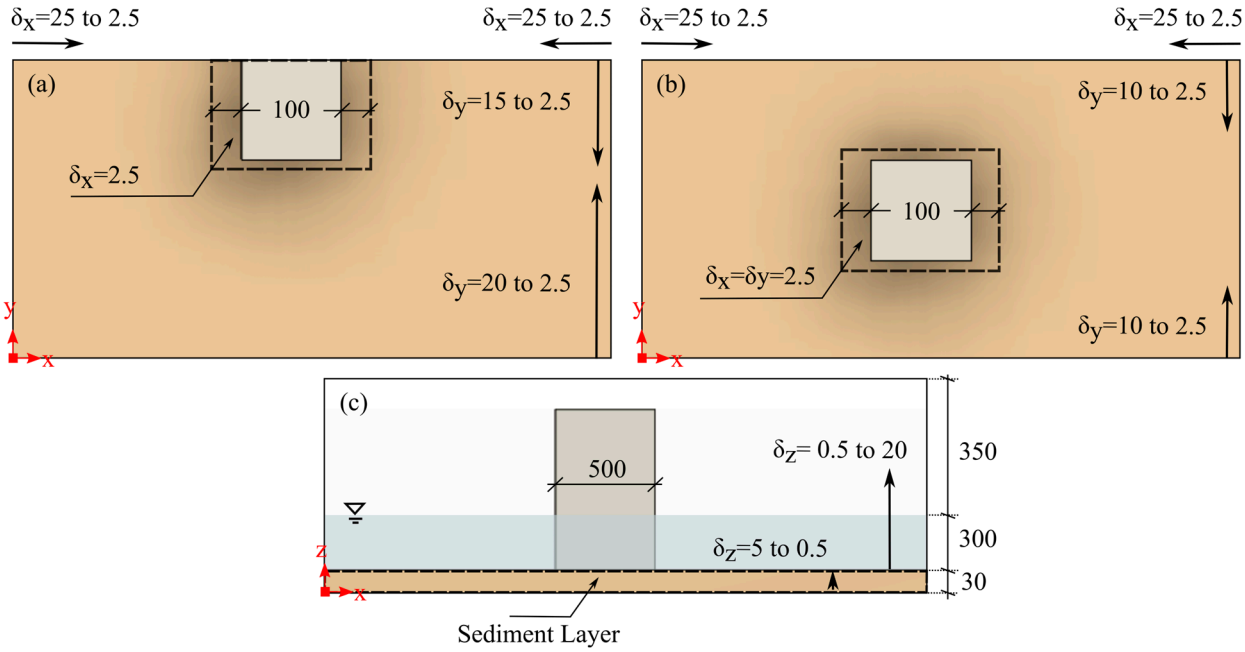

Figure 3. Final mesh of NWF for both models. (**a**) side; (**b**) center layouts on $x - y$ plane; (**c**) both layouts on $x - z$ plane. All units are in mm. Not to scale.

3.4. Validation

The accuracy of the numerical models is evaluated in both time and frequency domains. The wave gauges and ADVs were replicated in the NWF as line probes at the same locations as those in the experiments.

Figure 4a,b illustrates the temporal variations of the free surface elevation (η) at three selected wave gauge positions—WG1, WG2, WG3, and WG4 for the side layout and WG1, WG2, WG3, and WG7 for the center layout. WG1 is the wave gauge closest to the wave maker in both layouts, illustrating the time series profile of the incident wave generated by the wave maker. The height of the solitary wave measured by WG1 is 0.097 m. The gauges WG2 and WG3 measure the surface fluctuations of the channeled flows in both layouts, and WG4 and WG7 are the gauges that are attached to the structure's seaside face for the side and center layouts, respectively. The IA values for η range between 0.9–1.0, indicating a good agreement (Table 1).

The streamwise (u), spanwise (v), and vertical (w) velocity components at the three ADV locations are shown in Figure 4c,d. The raw velocity data were filtered to remove the noise resulting from potential air entrainment and suspended sediment. The noise was filtered based on a correlation $\geq$ 75% and signal-to-noise ratio (SNR) $\geq$ 10–15. Compared to the free surface elevations, the velocity field has lower IA values, especially for spanwise and vertical velocity components (Table 1). These discrepancies are attributed to the residual noise in the measured data. The lowest IAs are related to the vertical velocity component, w, which is considerably small compared to the other two velocity components. Overall, a satisfactory performance was achieved.

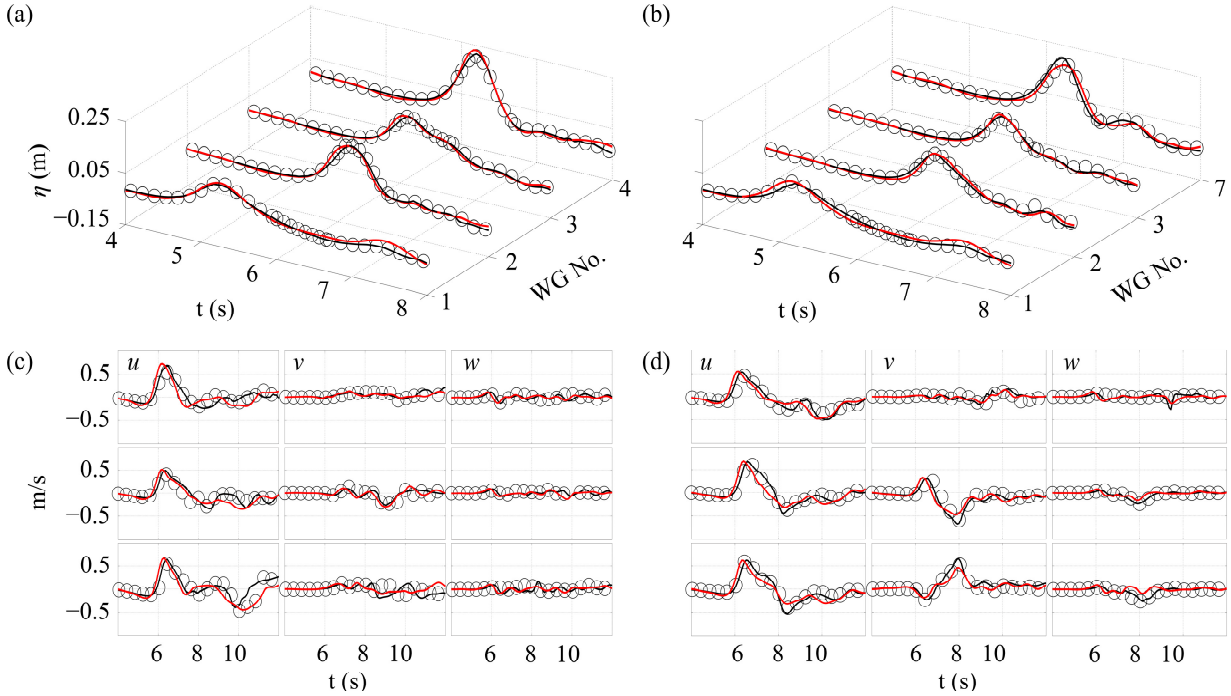

Figure 4. Comparison of measured (gray circles) and computed free surface elevations (η) and velocity components: (**a**–**c**) side; (**b**–**d**) center layout. Red and black solid lines represent SedWaveFoam and FLOW-3D results, respectively.

Table 1. Index of agreement (IA) for free surface elevations and velocity components.

		WG1	**WG2**	**WG3**	**WG4**	**WG5**	**WG6**	**WG7**	**WG8**	
SedWaveFoam	Side	0.974	0.980	0.978	0.977	0.966	0.959	0.951	0.944	
	Center	0.971	0.975	0.977	0.973	0.964	0.953	0.949	0.944	
FLOW-3D	Side	0.998	0.985	0.982	0.969	0.988	0.976	0.982	0.977	
	Center	0.989	0.979	0.978	0.965	0.986	0.902	0.978	0.963	
		ADV1			**ADV2**			**ADV3**		
		u	v	w	u	v	w	u	v	w
SedWaveFoam	Side	0.912	0.685	0.661	0.925	0.784	0.545	0.894	0.681	0.554
	Center	0.923	0.798	0.653	0.949	0.726	0.671	0.905	0.714	0.608
FLOW-3D	Side	0.937	0.738	0.646	0.934	0.751	0.671	0.909	0.686	0.589
	Center	0.972	0.773	0.642	0.958	0.779	0.701	0.927	0.724	0.614

3.5. Model Calibration

The sediment transport module of FLOW-3D is case specific, which requires careful calibration and validation through several parameters such as the entrainment parameter, α_i; bedload transport model type; and turbulence scheme. The following subsections provide an in-depth calibration analysis using the abovementioned parameters.

3.5.1. Entrainment Parameter

Wake vortices are the main driving mechanism of scouring around structures under wave action, where suspended sediment transport is identified as the major transport mode [11,12,17,35,36,60]. Therefore, accurately replicating the suspended sediment concentration in the FLOW-3D model is crucial. To achieve reliable results, it is imperative to adjust the lifting velocity (Equation (11)), which is a function of the entrainment parameter (α).

Figure 5 shows the comparisons of the measured and predicted bed elevation (S) using three different entrainment parameters ranging from α = 0.018 (default) to $\alpha = 0.18$ at a particular time instant ($t = 15$ s) as an example. The predicted bed elevations for both layouts did not align well with the experimental results when the recommended value of the entrainment parameter, α = 0.018, was employed. Of the parameters tested, $\alpha = 0.18$ was found to provide the best outcome based on the comparison of the scour and deposition patterns as well as the maximum scour depths for both layouts (Figure 5).

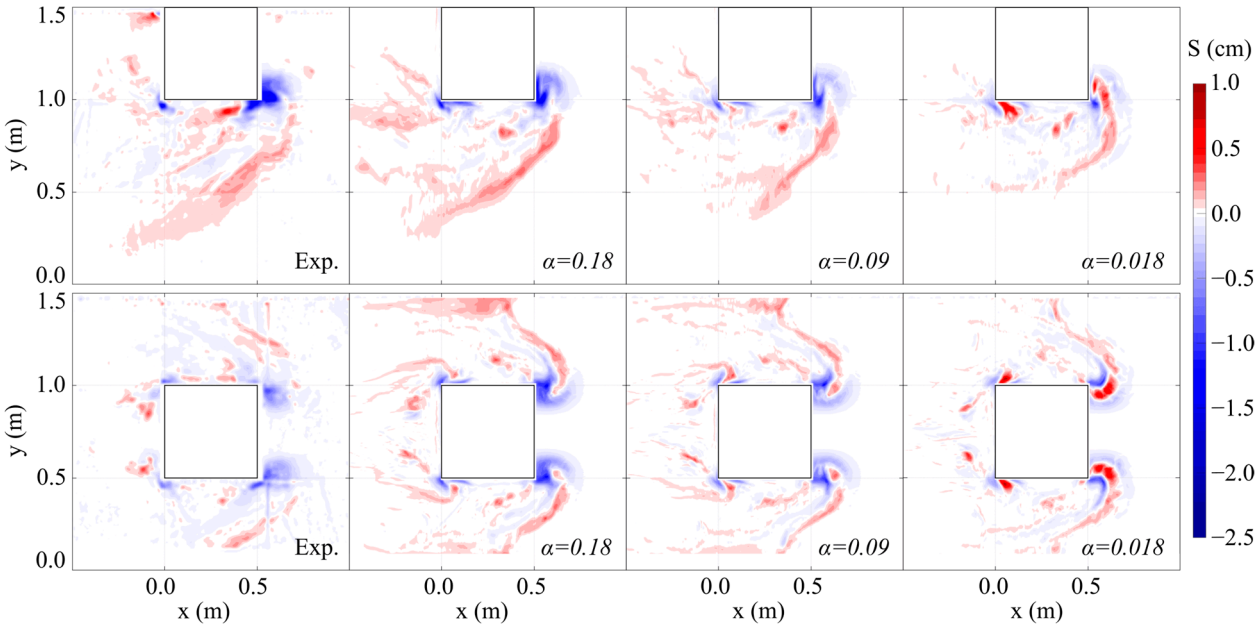

Figure 5. Plan view of sandy bed at $t = 15$ s. Upper panels: side layout. Lower panels: center layout. The figure compares the measured and predicted bed elevations using three different α values.

3.5.2. Bedload Transport Model

FLOW-3D considers a packed bed as an erodible solid object, with its morphological changes governed by the conservation of sediment mass. Bedload transport is described as sediment moving laterally along the channel without being suspended. The model computes bedload transport in each mesh cell using equations from Nielsen [54], van Rijn [55], or Meyer-Peter and Müller [56]. These three equations were compared to determine the most applicable approach for the default roughness coefficient, $c_{rough} = k_s/d_{50} = 2.5$, where $d_{50} = 0.27$ mm (Figure 6). The Nielsen equation produced the best results, with the scour and deposition trends closely matching the experimental data. The predictions were consistent with the center layout.

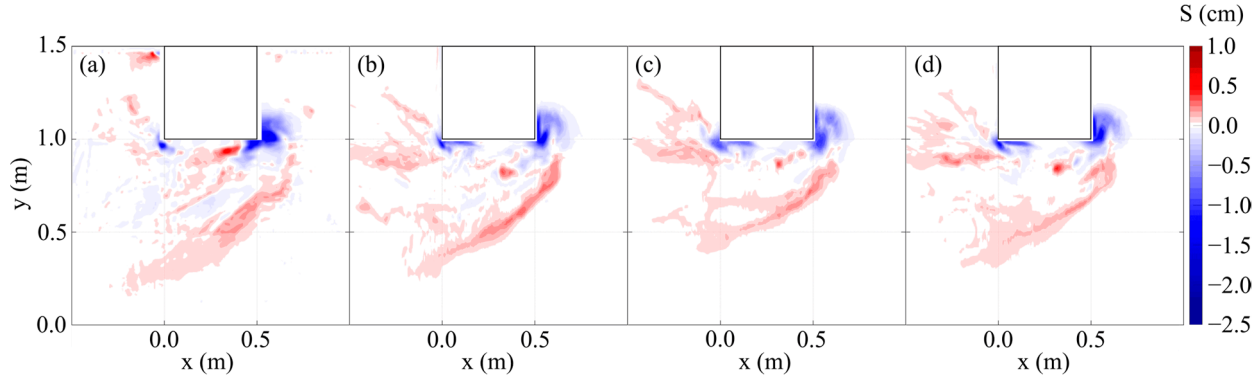

Figure 6. Plan view of sandy bed at $t = 15$ s. (**a**) Measurement; FLOW-3D results obtained using equations of (**b**) Nielsen; (**c**) van Rjin; (**d**) Meyer-Peter–Müller.

3.5.3. Turbulence Scheme

The simulations were carried out using four different turbulence schemes: (i) the two-equation $k - \omega$ model [61–63]—suitable for modeling free shear flows with streamwise pressure gradients like spreading jets, wakes, and plumes; (ii) the two-equation $k - \varepsilon$ model [64]—dynamically calculates the turbulent mixing length and thus useful for a wide range of flows [65]; (iii) the renormalized group (RNG) $k - \varepsilon$ model [66,67]—extends the capabilities of the standard $k - \varepsilon$ model and provide a better coverage for transitionally turbulent flows; (iv) the LES model—resolves most of the turbulent fluctuations directly, thus requiring much more computational resources compared to the two-equation models. Figure 7 highlights the implication of these four turbulence schemes in terms of scour and depositions in the vicinity of the structure for the side layout.

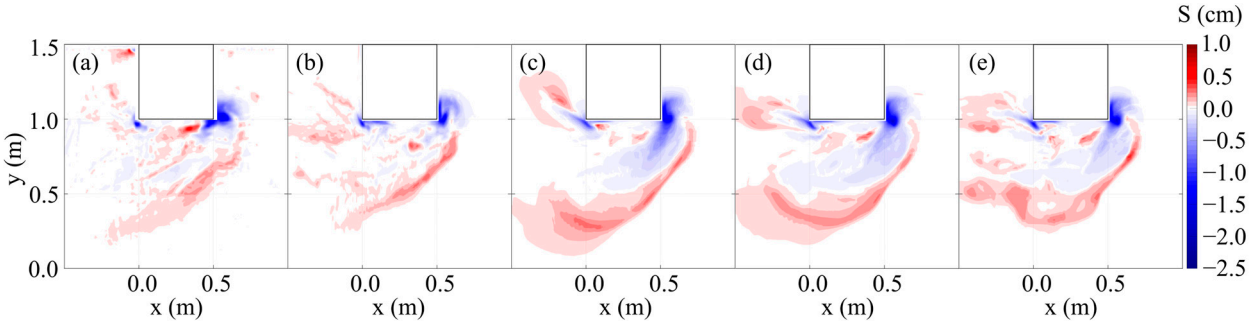

Figure 7. Plan view of sandy bed at $t = 15$ s. (**a**) Measurement; FLOW-3D results for different turbulence schemes: (**b**) LES; (**c**) RNG; (**d**) $k - \varepsilon$; (**e**) $k - \omega$.

The LES scheme predicted both seaside and leeside non-equilibrium scour reasonably well, while the RNG, $k - \varepsilon$, and $k - \omega$ schemes struggled to effectively predict the depositions around the structure. Instead, these approaches computed large scour footprints on the leeside of the structure that extended along a $\sim 45^{\circ}$ line towards the center of the NWF—a phenomenon that was not observed during the experiments. Similar results were obtained for the center layout, where the LES scheme provided the best result with respect to non-equilibrium scour prediction.

In summary, the calibration analysis indicates that FLOW-3D produced the best bed elevation predictions with $\alpha_i = 0.18$, the Nielsen [54] bed load transport model, and LES as the turbulence scheme.

4. Results and Discussion

A comparative analysis of the SedWaveFoam and FLOW-3D performances is presented in the following.

In Figure 8, we observe the spatial distributions of the instantaneous surface horizontal velocity, $U = \sqrt{u^2 + v^2}$, and the vertical velocity component, w, at two different depths: $h/3$ m above the sandy bed and on the surface of the sandy bed. The most intense vortex motion is observed between $t = 7$ s and $t = 8$ s, shortly after the wave impinges on the structure. The spatial distributions of U and w simulated by both models are quite similar for these time instants. The highest surface horizontal velocities are observed in the area near the vortex cores, which become less intense as the water level rises under the crest of the solitary wave.

Both the surface horizontal and vertical velocities above the bed increase as the wake vortex moves along its spiral trajectory (Figure 8a,c) for both layouts. However, the same trend is not observed on the bed surface, where the magnitude of these velocities does not change significantly with respect to time (Figure 8b,d). These findings suggest that changes in vortex intensity do not necessarily have an impact on sediment suspension above a certain elevation from the bed.

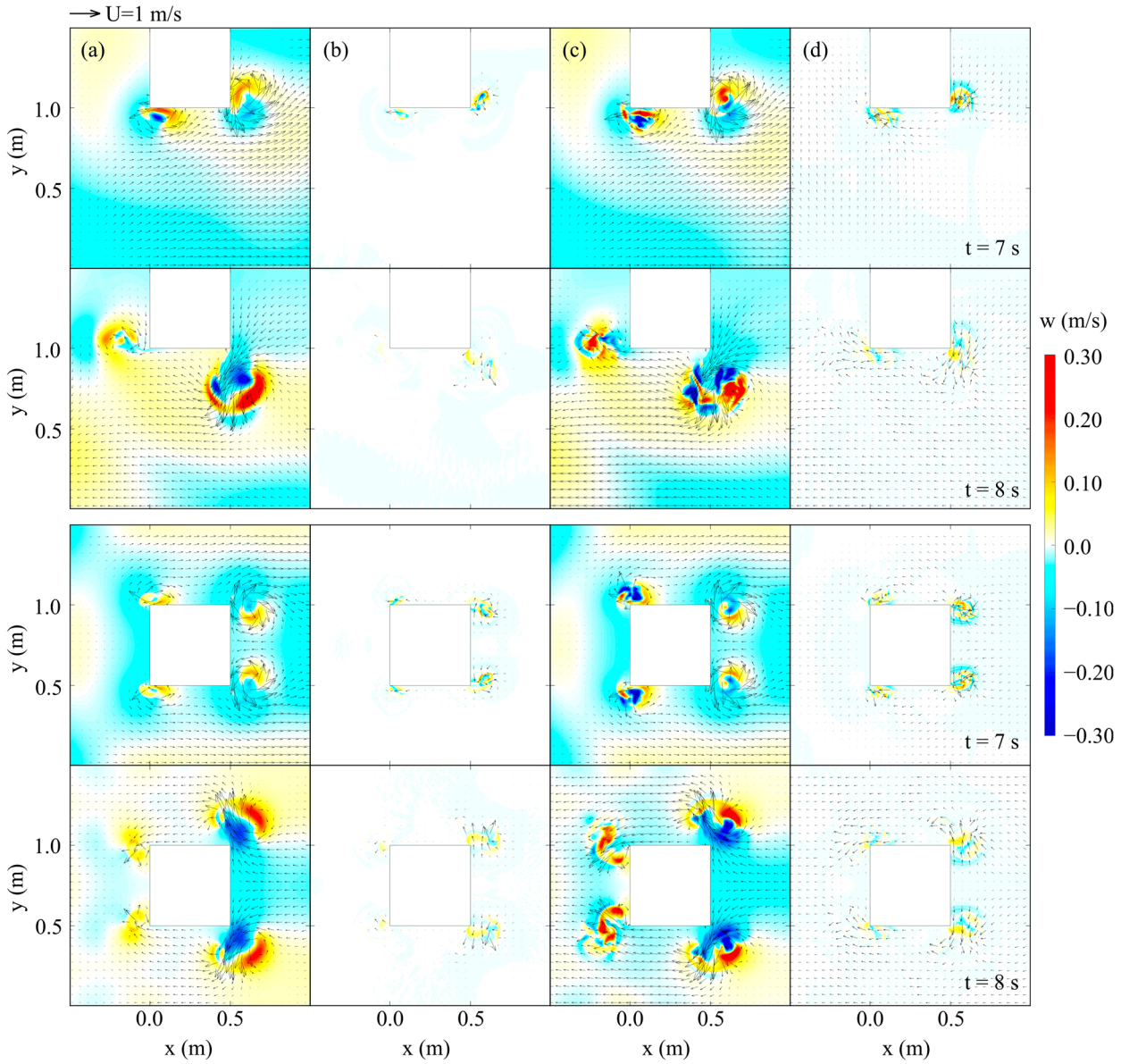

Figure 8. Spatial distributions of U and w at $t = 7$ s and $t = 8$ s, extracted from (**a**,**c**) $h/3$ m above bed; (**b**,**d**) bed surface. (**a**,**b**) and (**c**,**d**) are SedWaveFoam and FLOW-3D results, respectively. Upper two panels: side layout. Lower two panels: center layout.

Figure 9 depicts the spatial distributions of the instantaneous surface horizontal velocity, U, and the out-of-plane vorticity, ω_z, extracted at the two different depths—$h/3$ m above the sandy bed and on the bed surface—at $t = 7$ s and $t = 8$ s. The spatial distribution of ω_z simulated by both models is very similar, where the intensity ranges from -30 Hz to 30 Hz. The clockwise (CW) and counterclockwise (CCW) spinning vorticities at $t = 8$ s—marked with hot and cold colors, respectively—are the vortex doublets (i.e., ω_{za} and $\omega_{za'}$; ω_{zb} and $\omega_{zb'}$). For the center layout, a symmetric pattern of vortex pairs is formed on both seaside and leeside, with the structure's centerline being the line of symmetry. The wake vortices, ω_{zb} and ω_{zc}, are found to be larger and more intense than the out-of-plane vortices, ω_{za} and ω_{zd}, that occur at the seaside of the structure. The CCW rotating out-of-plane vortices follow a spiral trajectory for both layouts. On the other hand, the formation of CW rotating vortices, $\omega_{z'}$, is attributed to the offshore-directed flow. These vortices adopt a path that is close to a 45° line.

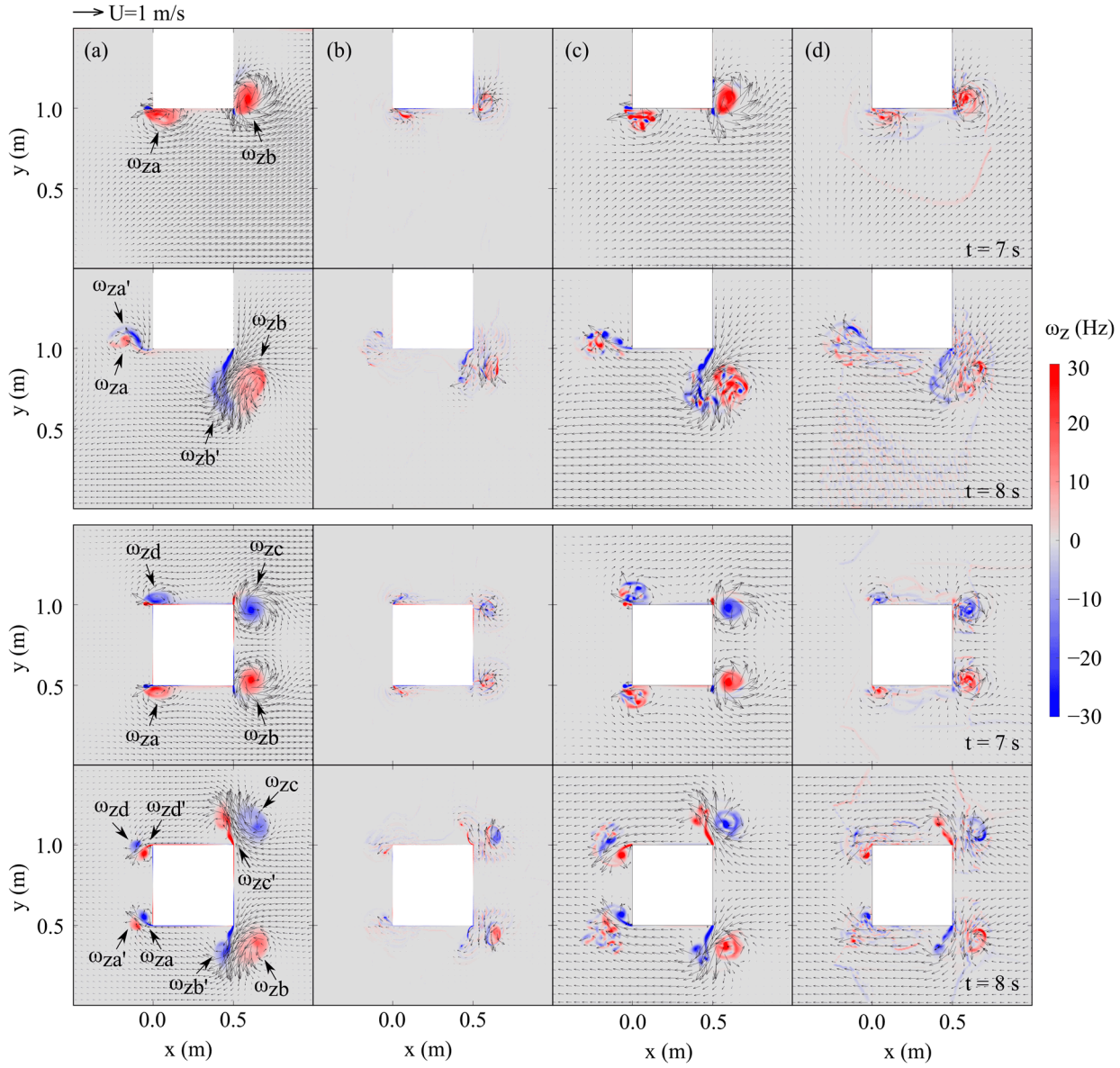

Figure 9. Spatial distributions of U and ω_z at $t = 7$ s and $t = 8$ s, extracted from (**a**,**c**) $h/3$ m above bed; (**b**,**d**) bed surface. (**a**,**b**) and (**c**,**d**) are SedWaveFoam and FLOW-3D results, respectively. Upper two panels: side layout. Lower two panels: center layout.

Figures 10 and 11 present the spatiotemporal variation in bed elevation and sediment volumetric concentration (ϕ^s) in the vicinity of the structure for both layouts. Here, the relative position of the bed within each cell is obtained by taking ϕ^s as 0.5 based on VOF method (Figures 10 and 11—upper panels). The values of ϕ^s range between 0 and 0.6 since the porosity of the sediment (i.e., the fluid fraction) is 0.4 (Figures 10 and 11—lower panels). As SedWaveFoam solves for the three phases, it treats sediment as a single separate phase in addition to air and water phases. Therefore, the instantaneous "spikes" ($S > 0$) in Figures 10a and 11a (upper panels) represent suspended sediment, which is included in the predicted bed elevation. FLOW-3D, on the other hand, employs the quadratic law of bottom shear stress and Equations (14)–(17) to estimate the bed load and suspended sediment concentration and generates separate outputs for bed elevation and sediment transport modes. Consequently, the FLOW-3D output does not reflect any instantaneous "spikes" (Figures 10b and 11b).

Both models predict that soon after the wave impingement on the structure, a significant amount of sediment is suspended near the edges, followed by the formation of scour holes. The highest suspended sediment concentration is confined within the lowest 30% of the water column (i.e., $z = -0.30$ m and $z = -0.22$ m) around the cores of the wake vortices. This can be attributed to the underprediction of the vortex-induced near-bed vertical velocity (w_n) by both models, which is unable to carry the suspended sediment further upward towards the free surface. Furthermore, between $t = 6$ s and $t = 8$ s, the dominant sediment transport mode is the suspended load, which is the determining factor denoting the deposition and/or erosion patterns.

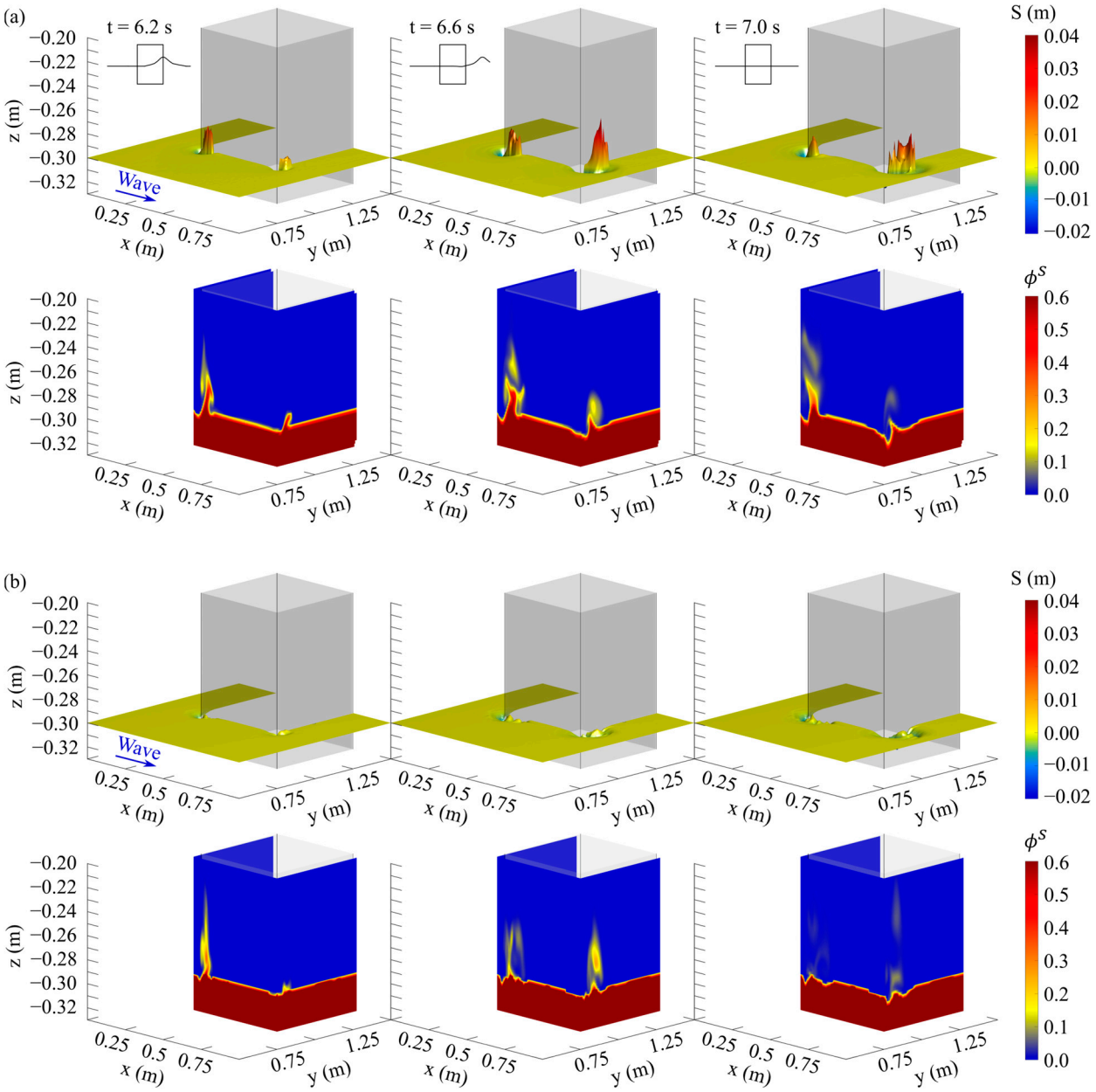

Figure 10. Bed elevation and suspended sediment concentration (ϕ^s) in the vicinity of the structure at various time instants for side layout. (**a**) SedWaveFoam results; (**b**) FLOW-3D results.

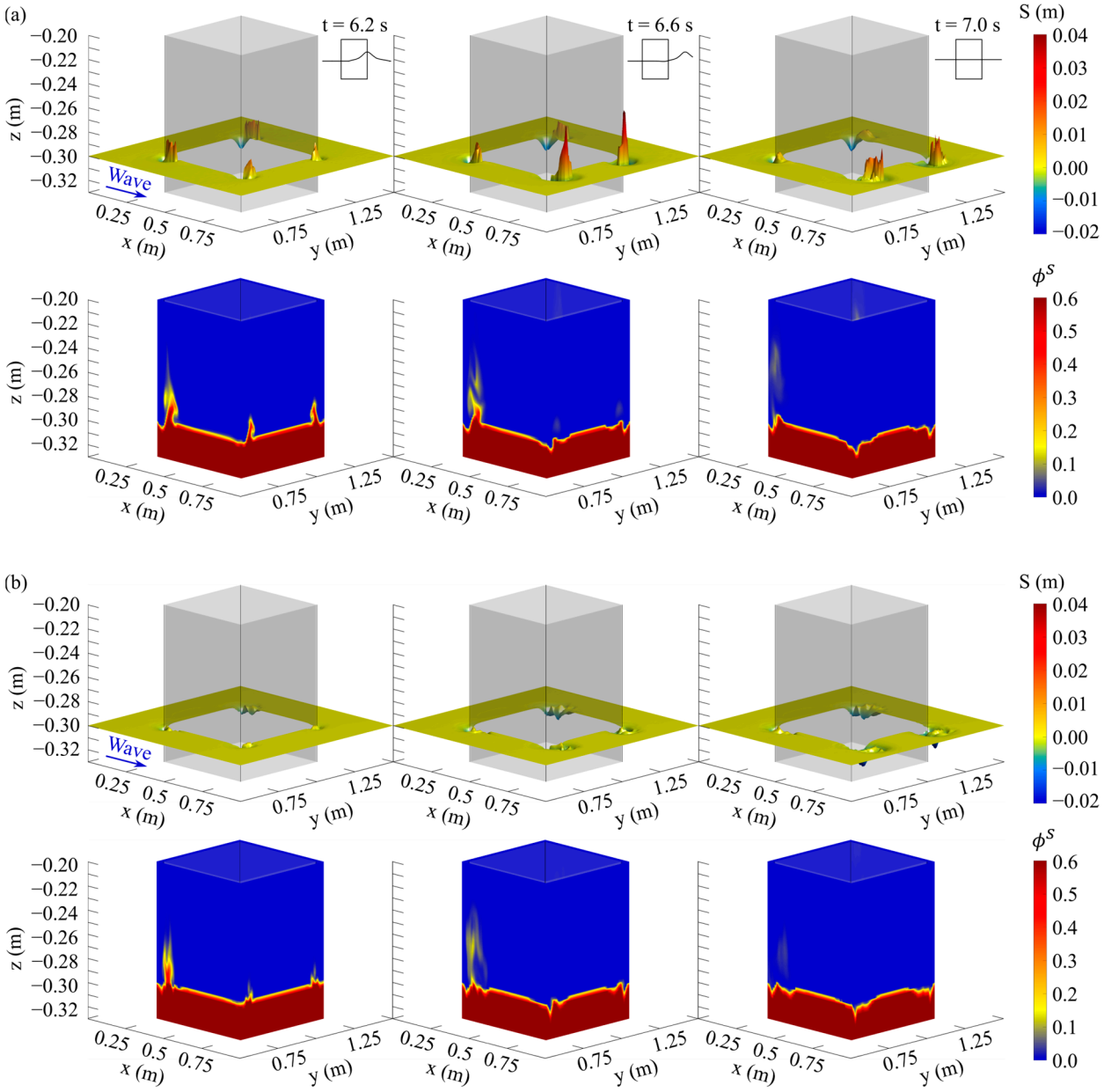

Figure 11. Bed elevation and suspended sediment concentration (ϕ^s) in the vicinity of the structure at various time instants for center layout. (**a**) SedWaveFoam results; (**b**) FLOW-3D results.

The suspended sediment concentration in the vicinity of the structure is relatively lower when the structure is placed in the center of the NWF (Figures 10b and 11b) owing to a less intense near-bed vorticity for the center layout (Figure 9b,d) compared to that of the side layout. Accordingly, the scour holes around the structure's edges are relatively shallower for the center layout, consistently predicted by two models (Figures 10a and 11a). The difference in the scour hole depths between the two layouts is more distinctive in the FLOW-3D predictions, possibly because the suspended sediment concentration is considerably lower than that predicted by SedWaveFoam.

The instantaneous suspended sediment concentrations at the leeside edge of the structure simulated by SedWaveFoam and FLOW-3D follow a similar trend for both layouts. The sediment that is captured by the out-of-plane vortex is carried up to $z = -0.22$ m and $z = -0.24$ m for the side and center layouts, respectively. On the other hand, the instantaneous suspended sediment concentrations at the seaside edge of the structure simulated by SedWaveFoam follow a different trend than that of FLOW-3D. The difference

can be attributed to the intensity of the wake vortex simulated by both models. In particular, for the center layout, the suspended sediment concentration simulated by SedWaveFoam is relatively higher, where it is carried up to $z = -0.28$ m.

Figure 12—upper panels depict the trajectories of the primary vortices and the plan view of sandy bed at $t = 15$ s for both layouts. The changes in the sandy bed morphology occur primarily along the vortex trajectories. The sediment mobilized by the near-bed vertical velocity (w_n) is entrapped by out-of-plane and wake vortices. The less intense out-of-plane vortices transport and deposit the sediment in the vicinity of the structure. On the other hand, as the wake vortices drift further seaward, they can no longer sustain their energy and start to dissipate, leaving sediment deposits along their trajectories. When the structure is placed on the side of the wave flume, the path of the out-of-plane vortices simulated by SedWaveFoam is quite similar to that of experiments (i.e., the dotted arrows), while the out-of-plane vortex trajectory simulated by FLOW-3D slightly differs from the measurements. The traces of the sediment deposits captured by the wake vortex and simulated by SedWaveFoam are oriented ~35 degrees (Figure 12a) with respect to the incident wave direction, while the wake vortex simulated by FLOW-3D travels along a nearly 45-degree trajectory (Figure 12b), consistent with the observations marked by the dotted arrows. For the center layout, the trajectory of the out-of-plane vortex pair bends towards the structure's seaside wall (Figure 12e), forming a thin layer of sediment deposit along the trajectory. On the other hand, the wake vortex pair follows a spiral path (Figure 12f), forming scour holes along the leeside edges, and depositing sediment along its trajectory. The vortex pair trajectories simulated by both models are quite similar to the observations. Contrary to the laboratory observations, SedWaveFoam predicts additional sediment deposits along the trajectory of the wake vortices for both layouts (Figure 12c,g). This is most likely due to the poor performance of the k − ε model, which underpredicts w_n. For the side layout, the predicted scour hole depth is lower than the measured value, whereas the model predicts deeper scour holes around the edges of the structure for the center layout. Both SedWaveFoam and FLOW-3D underestimate the depth of the scour holes at the structure's edges for the side layout, whereas they overpredict the scour holes for the center layout (Figure 12d,h). Overall, it is seen that FLOW-3D performs better than SedWaveFoam at predicting the final bed elevation. This finding is mainly attributed to the LES turbulence scheme used in FLOW-3D, which assists the model in resolving smaller eddies that may still contribute to bed evolution.

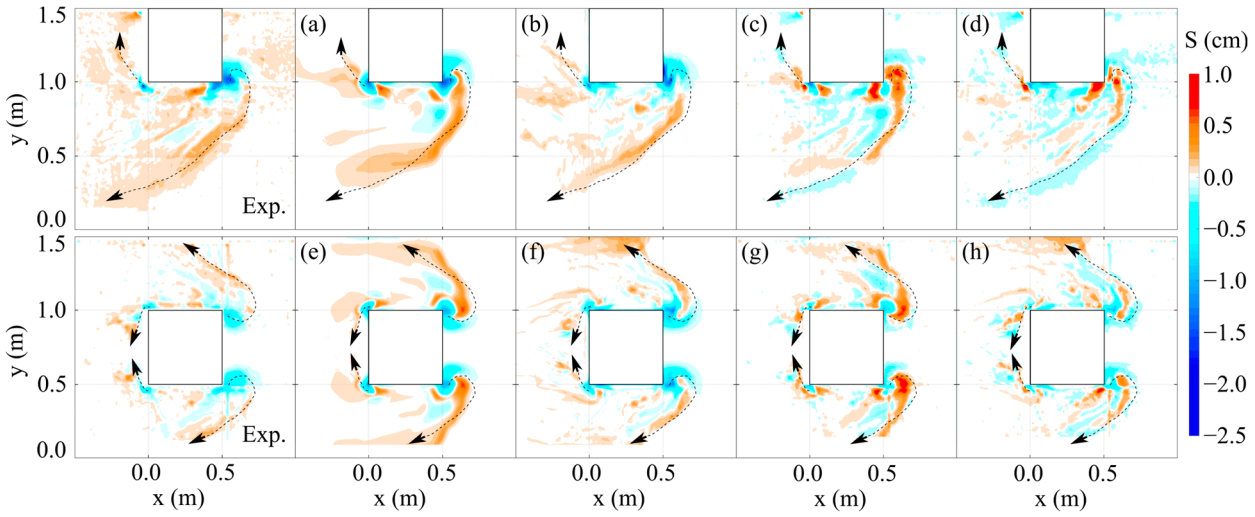

Figure 12. Plan view of sandy bed at $t = 15$ s. Upper panels: side layout. Lower panels: center layout. (**a**,**e**) SedWaveFoam results; (**b**,**f**) FLOW-3D results; (**c**,**g**) difference between SedWaveFoam results and measurement; (**d**,**h**) difference between FLOW-3D results and measurement.

The instantaneous bed elevation along the vortex trajectories at $t = 15$ s, extracted from the measured final bed elevation, for both seaside and leeside of the structure is plotted in Figure 13 for both layouts. The inconsistencies between the predicted and actual bed elevations, Δz, are calculated by subtracting the actual bed elevation from those simulated by the two models. The shaded panels in Figure 13 present Δz, where the dashed red and black lines represent the deviation of the SedWaveFoam and FLOW-3D simulations from the measurements, respectively. The scour induced by both out-of-plane and wake vortices is followed by areas of mild deposition along the vortex trajectories. The vortex effect on the bottom is inferred by comparing the scour depth for both layouts. The near-bed vorticity is relatively higher for the side layout (Figure 9), leading to deeper scour holes both at the leeside and seaside of the structure. SedWaveFoam slightly overestimates deposits along vortex trajectories for both layouts. FLOW-3D, on the other hand, performs better in predicting deposits beneath the vortex paths at the structure's seaside for both layouts; however, the deposits towards the structure's leeside are underestimated for the side layout. Both models fail to accurately predict the vortex-induced scour, which is most noticeable at the structure's seaside for the side layout.

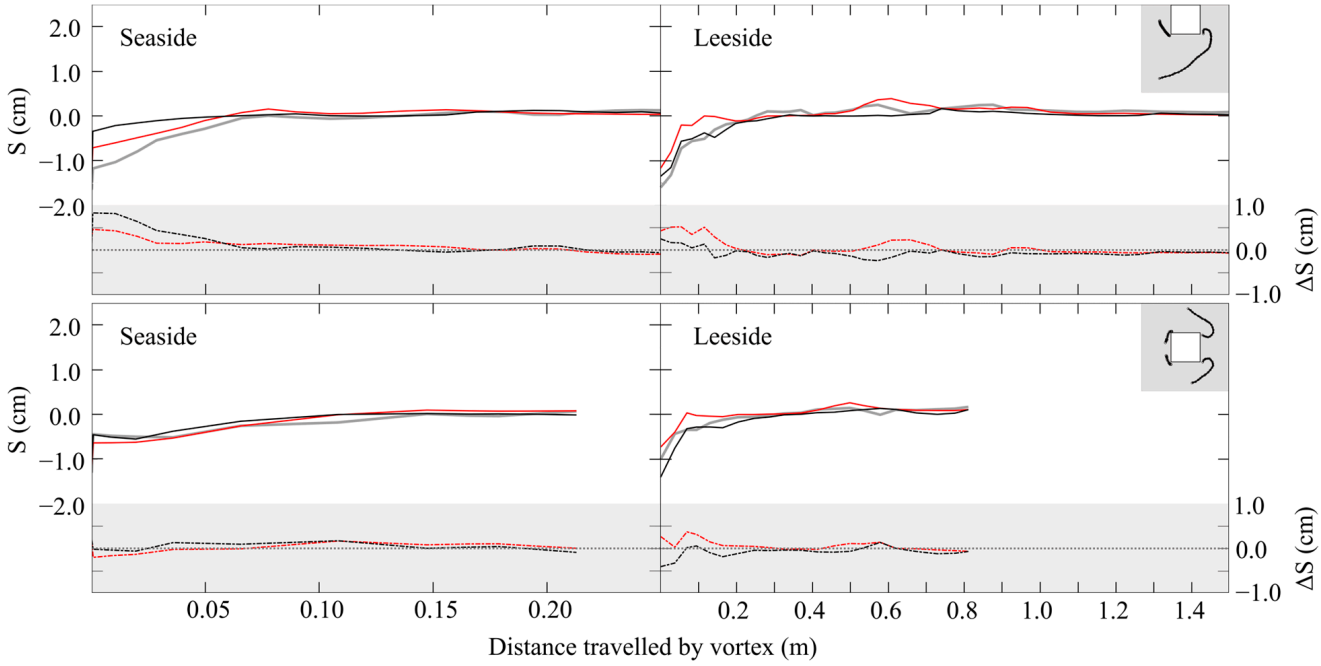

Figure 13. Elevation of sandy bed along vortex trajectories at seaside and leeside of the structure at $t = 15$ s. Upper panels: side layout. Lower panels: center layout. Gray, red, and black lines represent measurement, SedWaveFoam, and FLOW-3D results, respectively.

The temporal evolution of the maximum scour depth on the seaside and leeside of the structure is shown in Figure 14, where the measured maximum scour at $t = 15$ s is denoted by "X". The scour holes generated by the wave impingement are backfilled after the wave passes the structure and the flow climate gets milder. The backfilling is more prominent in SedWaveFoam results, where the initial scour depth is considerably reduced between $t = 7$ s and $t = 8$ s. The scour depth on the seaside is relatively constant until $t = 13$ s before it undergoes a sudden increase. The scour depth then remains constant, implying that stability is reached. On the other hand, the scour hole formed at the leeside of the structure is disrupted at $t = 10.5$ s both for the side and center layout, where an increase in scour depth is followed by abrupt backfilling. This is probably associated with the settling of sand that was previously suspended by the strong wake vortices during wave impingement. FLOW-3D simulations do not reflect the backfilling of the initially

formed scour. The scour depth reaches its maximum depth at $t = 8$ s for both layouts and does not show any variation until $t = 15$ s.

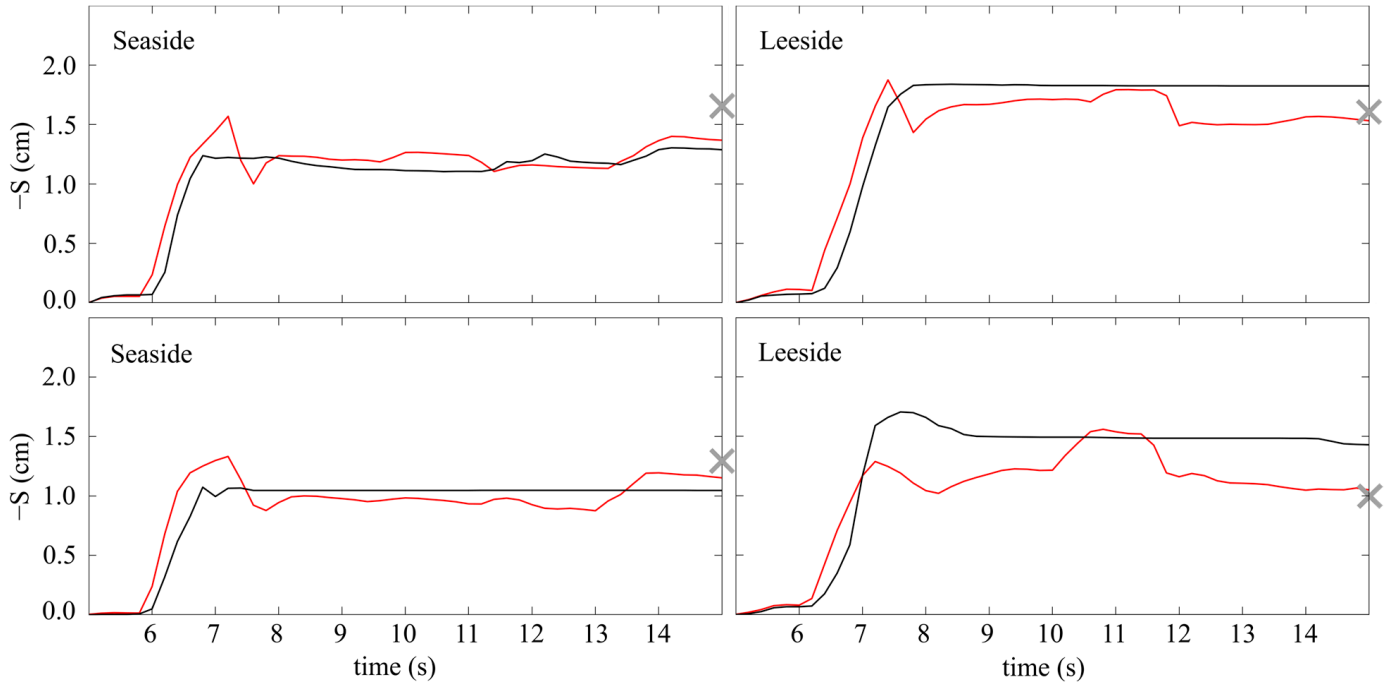

Figure 14. Temporal evolution of maximum scour depth at seaside and leeside of the structure. Upper panels: side layout. Lower panels: center layout. Red and black lines represent SedWaveFoam and FLOW-3D results, respectively. X represents the measured maximum scour depth.

SedWaveFoam manages to capture the backfilling process that is observed during the experiments after the wave impingement and predicts the maximum scour depth with reasonable accuracy. FLOW-3D, on the other hand, performs poorly and fails to accurately predict the maximum scour depth at $t = 15$ s. Overall, SedWaveFoam performs better in capturing the temporal evolution of the maximum scour depth for both layouts.

The cross-sectional view of sandy bed along two lines, i.e., line A–A, and D–D, at $t = 15$ s is given in Figure 15. The cross-sections are taken 3 cm away from the structure for both layouts. SedWaveFoam underestimates the seaside and leeside scour depths for the side layout and predicts depositions in the vicinity of the structure, which are not observed in the experiments for both layouts. The disparity seen between the measurement and SedWaveFoam results is most likely due to k − ε model, which inherently underestimates the intensity of the vortex in the case of adverse pressure caused by flow blockage [61,68–70]. These vortices are unlikely to carry the trapped sediment away from the structure, resulting in the depositions depicted in Figure 15. Compared to SedWaveFoam, FLOW-3D demonstrates a better performance in predicting the cross-sectional bed evolution. For both layouts, the model predicts no depositions near the structure, while the scour depth is slightly underpredicted for the side layout. Both models overestimate the scour depth for the center layout. This is attributed to the predicted near-bed vorticities, which are relatively higher compared to the experiments.

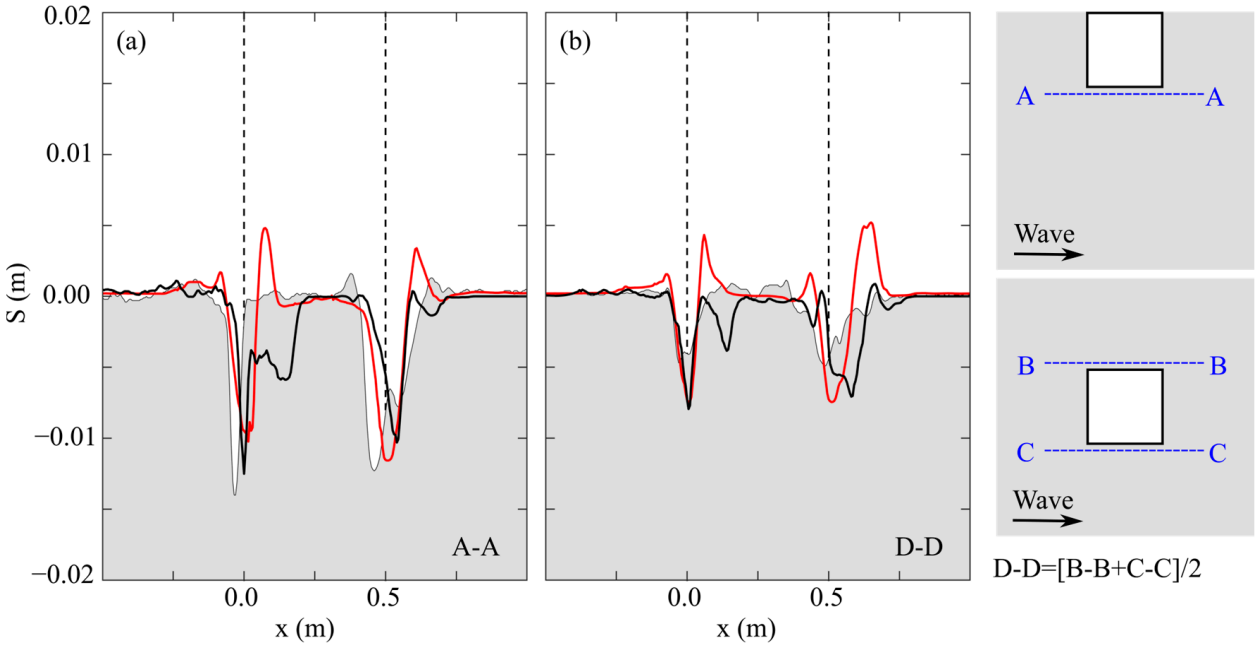

Figure 15. Cross-sectional view of sandy bed along line A–A and D–D at $t = 15$ s: (**a**) side layout; (**b**) center layout. Gray, red, and black solid lines represent measurement, SedWaveFoam, and FLOW-3D results, respectively. Gray dashed line represents the structure.

5. Conclusions

The present study presents a thorough analysis of the accuracy of two different approaches in estimating the non-equilibrium scour around a non-slender structure exposed to a transient wave as well as a detailed description of the scouring and deposition processes based on laboratory observations and numerical simulations. The first numerical method treats the sediment layer as a separate phase and directly solves continuity and momentum equations for the sediment, water, and air phases by implementing the $k - \varepsilon$ turbulence scheme. The second numerical approach estimates sediment transport using conventional bedload and suspended load methods where the quadratic law of bottom shear stress for 3D turbulent flow is assumed and the LES scheme is utilized.

The most intense vortex motion is seen immediately after the wave impinges on the structure. The area around the vortex cores has the highest surface horizontal velocities, which decrease in intensity as water depth increases. For both layouts, the surface horizontal and vertical velocities increase as the wake vortex moves along its spiral trajectory. The same pattern is not seen near the sandy bed, where the magnitude of these velocities does not vary dramatically over time. The wake vortices are larger and more intense than the out-of-plane vortices that form at the structure's seaside. The predicted suspended sediment concentration is mostly confined between $z = -0.30$ m and $z = -0.22$ m, which is attributed to the underestimation of vortex-induced near-bed vertical velocities by both SedWaveFoam and FLOW-3D. It is found that the suspended sediment concentration in the vicinity of the structure is relatively lower when the structure is placed in the center of the NWF. This is expected given that the near-bed vorticity magnitudes of the vortex pairs in the center layout are smaller than those in the side layout. As a result, the scour around the structure's edges is deeper when the structure is placed on the side of the NWF. SedWaveFoam overestimates the deposits along vortex trajectories for both layouts, whereas FLOW-3D satisfactorily predicts scour and depositions beneath vortex paths. When the wave passes the structure and the flow climate becomes milder, the scour holes caused by the wave impingement are backfilled. SedWaveFoam can estimate the maximum scour depth and capture this backfilling. FLOW-3D results, on the other hand, do not reflect the backfilling that is seen during the experiments and the model fails to accurately predict

the maximum scour depth. SedWaveFoam results indicate noticeable depositions along the cross-sections taken 3 cm away from the structure. These depositions are not observed in the experiments for both layouts. Both SedWaveFoam and FLOW-3D underpredict the scour depth for the side layout and overestimate the scour depth for the center layout.

No clear-cut case can be made for the advantages of utilizing any of the two different approaches based on the available evidence because the capabilities of SedWaveFoam and FLOW-3D in predicting the non-equilibrium scour for a low *KC* number vary greatly. Each model has its pros and cons, which were covered in detail in the preceding sections, and the results discussed here do not support the use of one model over another. However, the unwanted depositions in the vicinity of the structure and along vortex trajectories simulated by SedWaveFoam suggest that incorporating LES into SedWaveFoam could be a viable approach for future model improvement. On the other hand, the two equation turbulence schemes embedded in FLOW-3D fail to procure reliable results regarding the evolution of the sandy bed and the LES scheme is strongly encouraged to reach more accurate results. Unlike SedWaveFoam, FLOW-3D requires careful calibration of the entrainment parameter for each test case to properly estimate the suspended sediment concentration and backfilling, which shows that the model is case specific and should be used with caution.

The results of this study are only applicable to the flow conditions, structure size, and placements considered. For definitive conclusions addressing the scour around non-slender square structures under transient wave conditions, a more thorough investigation including a wider variety of flow conditions, structure dimensions, and layouts is required.

Author Contributions: Conceptualization, D.V.S., E.S. and A.F.; Methodology, D.V.S. and E.S.; Software, D.V.S. and T.-J.H.; Investigation, D.V.S.; Resources, D.V.S. and A.F.; Data curation, D.V.S. and E.S.; Writing—original draft, D.V.S.; Writing—review & editing, E.S., A.F. and T.-J.H.; Visualization, D.V.S. and E.S. All authors have read and agreed to the published version of the manuscript.

Funding: This material is based upon work supported by the National Science Foundation under grant no. CNS 09-23050. The authors acknowledge funding from the National Sciences Foundation through grants CMMI-2050798 and CMMI-2050854.

Institutional Review Board Statement: Not applicable.

Informed Consent Statement: Not applicable.

Data Availability Statement: Data are contained within the article.

Acknowledgments: FLOW-3D HYDRO software was made available through the FLOW-3D Academic Program.

Conflicts of Interest: The authors declare no conflict of interest.

References

1. Larsen, B.E.; Fuhrman, D.R.; Baykal, C.; Sumer, B.M. Tsunami-induced scour around monopile foundations. *Coast. Eng.* **2017**, *129*, 36–49. [CrossRef]
2. Williams, I.A.; Fuhrman, D.R. Numerical simulation of tsunami-scale wave boundary layers. *Coast. Eng.* **2016**, *110*, 17–31. [CrossRef]
3. Breusers, H.N.C.; Nicollet, G.; Shen, H. Local scour around cylindrical piers. *J. Hydraul. Res.* **1977**, *15*, 211–252. [CrossRef]
4. Carreiras, J.; Larroudé, P.; Seabra-Santos, F.; Mory, M. Wave scour around piles. In Proceedings of the 27th International Conference on Coastal Engineering 2000, Sydney, Australia, 16–21 July 2000; pp. 1860–1870.
5. Carreiras, J.; Carmo, J.D.; Seabra-Santos, F. Settlement of vertical piles exposed to waves. *Coast. Eng.* **2003**, *47*, 355–365. [CrossRef]
6. Dey, S.; Sumer, B.M.; Fredsøe, J. Control of scour at vertical circular piles under waves and current. *J. Hydraul. Eng.* **2006**, *132*, 270–279. [CrossRef]
7. Dey, S.; Helkjær, A.; Sumer, B.M.; Fredsøe, J. Scour at vertical piles in sand-clay mixtures under waves. *J. Waterw. Port Coast. Ocean Eng.* **2011**, *137*, 324–331. [CrossRef]
8. Kobayashi, T. 3-D Analysis of flow around a vertical cylinder on a scoured bed. In Proceedings of the 23rd International Conference on Coastal Engineering, Venice, Italy, 4–9 October 1992; pp. 3482–3495.
9. Kobayashi, T.; Oda, K. Experimental study on developing process of local scour around a vertical cylinder. In Proceedings of the 24th International Conference on Coastal Engineering, Kobe, Japan, 23 October 1994; pp. 1284–1297. [CrossRef]

10. Raaijmakers, T.; Rudolph, D. Time-dependent scour development under combined current and waves conditions-laboratory experiments with online monitoring technique. In Proceedings of the 4th International Conference on Scour and Erosion, ICSE, Tokyo, Japan, 5–7 November 2008; pp. 152–161.
11. Sumer, B.M.; Christiansen, N.; Fredsoe, J. Time scale of scour around a vertical pile. In Proceedings of the ISOPE International Ocean and Polar Engineering Conference, San Francisco, CA, USA, 14–19 June 1992; p. ISOPE-I-92-259.
12. Sumer, B.M.; Fredsøe, J.; Christiansen, N. Scour around vertical pile in waves. *J. Waterw. Port Coast. Ocean Eng.* **1992**, *118*, 15–31. [CrossRef]
13. Sumer, B.M.; Christiansen, N.; Fredsøe, J. Influence of cross section on wave scour around piles. *J. Waterw. Port Coast. Ocean Eng.* **1993**, *119*, 477–495. [CrossRef]
14. Sumer, B.M.; Fredsøe, J.; Christiansen, N.; Hansen, S.B. Bed shear stress and scour around coastal structures. In Proceedings of the 24th International Conference on Coastal Engineering, Kobe, Japan, 23 October 1994; pp. 1595–1609.
15. Sumer, B.M.; Fredsøe, J. Scour around pile in combined waves and current. *J. Hydraul. Eng.* **2001**, *127*, 403–411. [CrossRef]
16. Sumer, B.M.; Fredsøe, J. Time scale of scour around a large vertical cylinder in waves. In Proceedings of the ISOPE International Ocean and Polar Engineering Conference, Kitakyushu, Japan, 26–31 May 2002; p. ISOPE-I-02-143.
17. Sumer, B.M.; Fredsøe, J. The mechanics of scour in the marine environment. In *Advanced Series on Ocean Engineering*; Word Scientific: Singapore, 2002.
18. Sumer, B.M. Mathematical modelling of scour: A review. *J. Hydraul. Res.* **2007**, *45*, 723–735. [CrossRef]
19. Whitehouse, R. *Scour at Marine Structures: A Manual for Practical Applications*; Thomas Telford: London, UK, 1998.
20. Zanke, U.C.; Hsu, T.-W.; Roland, A.; Link, O.; Diab, R. Equilibrium scour depths around piles in noncohesive sediments under currents and waves. *Coast. Eng.* **2011**, *58*, 986–991. [CrossRef]
21. Rance, P.J. *The Potential for Scour around Large Objects, One-Day Seminar of Scour Prevention Techniques around Offshore Structures*; Society for Underwater Technology: London, UK, 1980; p. 41.
22. Nakamura, T.; Kuramitsu, Y.; Mizutani, N. Tsunami scour around a square structure. *Coast. Eng. J.* **2008**, *50*, 209–246. [CrossRef]
23. McGovern, D.; Todd, D.; Rossetto, T.; Whitehouse, R.; Monaghan, J.; Gomes, E. Experimental observations of tsunami induced scour at onshore structures. *Coast. Eng.* **2019**, *152*, 103505. [CrossRef]
24. Kato, F.; Sato, S.; Yeh, H. Large-scale experiment on dynamic response of sand bed around a cylinder due to tsunami. In Proceedings of the 27th International Conference on Coastal Engineering 2000, Sydney, Australia, 16–21 July 2000; pp. 1848–1859.
25. Mehrzad, S.; Nistor, I.; Rennie, C.D. Experimental modeling of supercritical flows induced erosion around structures. In Proceedings of the 6th International Conference Application of Physical Modeling in Coastal and Port Engineering and Science, Ottawa, ON, Canada, 10–13 May 2016; pp. 1–13.
26. Briganti, R.; Musumeci, R.E.; van der Meer, J.; Romano, A.; Stancanelli, L.M.; Kudella, M.; Akbar, R.; Mukhdiar, R.; Altomare, C.; Suzuki, T.; et al. Wave overtopping at near-vertical seawalls: Influence of foreshore evolution during storms. *Ocean Eng.* **2022**, *261*, 112024. [CrossRef]
27. Slingerland, R.L. Numerical models and simulation of sediment transport and deposition. In *Sedimentology: Encyclopedia of Earth Science*; Springer: Berlin/Heidelberg, Germany, 1978.
28. Henderson, S.M.; Allen, J.S.; Newberger, P.A. Nearshore sandbar migration predicted by an eddy-diffusive boundary layer model. *J. Geophys. Res. Ocean.* **2004**, *109*, C06024. [CrossRef]
29. Kranenburg, W.M.; Ribberink, J.S.; Uittenbogaard, R.E.; Hulscher, S.J.M.H. Net currents in the wave bottom boundary layer: On waveshape streaming and progressive wave streaming. *J. Geophys. Res. Earth Surf.* **2012**, *117*, F03005. [CrossRef]
30. Kranenburg, W.M.; Ribberink, J.S.; Schretlen, J.J.L.M.; Uittenbogaard, R.E. Sand transport beneath waves: The role of progressive wave streaming and other free surface effects. *J. Geophys. Res. Earth Surf.* **2013**, *118*, 122–139. [CrossRef]
31. Kim, Y.; Cheng, Z.; Hsu, T.; Chauchat, J. A Numerical study of sheet flow under monochromatic nonbreaking waves using a free surface resolving eulerian two-phase flow model. *J. Geophys. Res. Ocean.* **2018**, *123*, 4693–4719. [CrossRef]
32. Fox, B.; Feurich, R. CFD analysis of local scour at bridge piers. In Proceedings of the Federal Interagency Sedimentation and Hydrologic Modeling SEDHYD Conference, Reno, NV, USA, 24–28 June 2019; pp. 24–28.
33. Le Quere, P.A.; Nistor, I.; Mohammadian, A. Numerical modeling of tsunami-induced scouring around a square column: Performance assessment of FLOW-3D and Delft3D. *J. Coast. Res.* **2020**, *36*, 1278–1291. [CrossRef]
34. Sogut, E.; Farhadzadeh, A. Scouring and loading of idealized beachfront building during overland flooding. *Coast. Eng. Proc.* **2020**, *28*, 7. [CrossRef]
35. Sogut, E.; Hsu, T.-J.; Farhadzadeh, A. Experimental and numerical investigations of solitary wave-induced non-equilibrium scour around structure of square cross-section on sandy berm. *Coast. Eng.* **2022**, *173*, 104091. [CrossRef]
36. Sogut, E.; Sogut, D.V.; Farhadzadeh, A. Experimental study of bed evolution around a non-slender square structure under combined solitary wave and steady current actions. *Ocean Eng.* **2022**, *266*, 112792. [CrossRef]
37. Munk, W.H. The solitary wave theory and its application to surf problems. *Ann. N. Y. Acad. Sci.* **1949**, *51*, 376–424. [CrossRef]
38. Chiew, Y.M.; Melville, B.W. Local scour around bridge piers. *J. Hydraul. Res.* **1987**, *25*, 15–26. [CrossRef]
39. Ballio, F.; Teruzzi, A.; Radice, A. Constriction effects in clear-water scour at abutments. *J. Hydraul. Eng.* **2009**, *135*, 140–145. [CrossRef]
40. Sumer, B.M. *Hydrodynamics around Cylindrical Structures*; World Scientific: Singapore, 2006; Volume 26.

41. Chauchat, J.; Cheng, Z.; Nagel, T.; Bonamy, C.; Hsu, T.-J. SedFoam-2.0: A 3-D two-phase flow numerical model for sediment transport. *Geosci. Model Dev.* **2017**, *10*, 4367–4392. [CrossRef]
42. Berberović, E.; van Hinsberg, N.P.; Jakirlić, S.; Roisman, I.V.; Tropea, C. Drop impact onto a liquid layer of finite thickness: Dynamics of the cavity evolution. *Phys. Rev. E* **2009**, *79*, 036306. [CrossRef]
43. Jacobsen, N.G.; Fuhrman, D.R.; Fredsøe, J. A wave generation toolbox for the open-source CFD library: OpenFoam®. *Int. J. Numer. Methods Fluids* **2012**, *70*, 1073–1088. [CrossRef]
44. A Drew, D. Mathematical Modeling of Two-Phase Flow. *Annu. Rev. Fluid Mech.* **1983**, *15*, 261–291. [CrossRef]
45. Kim, Y.; Mieras, R.S.; Cheng, Z.; Anderson, D.; Hsu, T.-J.; Puleo, J.A.; Cox, D. A numerical study of sheet flow driven by velocity and acceleration skewed near-breaking waves on a sandbar using SedWaveFoam. *Coast. Eng.* **2019**, *152*, 103526. [CrossRef]
46. Cheng, Z.; Hsu, T.-J.; Calantoni, J. SedFoam: A multi-dimensional Eulerian two-phase model for sediment transport and its application to momentary bed failure. *Coast. Eng.* **2017**, *119*, 32–50. [CrossRef]
47. Hsu, T.-J.; Hanes, D.M. Effects of wave shape on sheet flow sediment transport. *J. Geophys. Res. Ocean.* **2004**, *109*, C05025. [CrossRef]
48. Flow Science. *FLOW-3D Version 12.0 User Manual*; Flow Science, Inc.: Santa Fe, NM, USA, 2019. Available online: https://www.flow3d.com (accessed on 12 March 2023).
49. Velioglu, D. Advanced Two- and Three-Dimensional Tsunami Models: Benchmarking and Validation. Ph.D. Dissertation, Middle East Technical University, Ankara, Turkey, 2017.
50. Hirt, C.W. A porosity technique for the definition of obstacles in rectangular cell meshes. In Proceedings of the 4th International Conference Ship Hydrodynamics, Washington, DC, USA, 24–27 September 1985.
51. Hirt, C.W.; Nichols, B.D. Volume of fluid (VOF) method for the dynamics of free boundaries. *J. Comput. Phys.* **1981**, *39*, 201–225. [CrossRef]
52. Mastbergen, D.R.; Van Den Berg, J.H. Breaching in fine sands and the generation of sustained turbidity currents in submarine canyons. *Sedimentology* **2003**, *50*, 625–637. [CrossRef]
53. Soulsby, R.L. Dynamics of marine sands: A manual for practical applications. *Oceanogr. Lit. Rev.* **1997**, *9*, 947.
54. Nielsen, P. *Coastal Bottom Boundary Layers and Sediment Transport*; World Scientific: Singapore, 1992; Volume 4.
55. Van Rijn, L.C. Sediment transport, part I: Bed load transport. *J. Hydraul. Eng.* **1984**, *110*, 1431–1456. [CrossRef]
56. Meyer-Peter, E.; Müller, R. Formulas for bed-load transport. In Proceedings of the IAHSR 2nd Meeting, Stockholm, Appendix 2, Stockholm, Sweden, 7 June 1948.
57. Higuera, P.; Lara, J.L.; Losada, I.J. Realistic wave generation and active wave absorption for Navier–Stokes models: Application to OpenFOAM®. *Coast. Eng.* **2013**, *71*, 102–118. [CrossRef]
58. Higuera, P.; Losada, I.J.; Lara, J.L. Three-dimensional numerical wave generation with moving boundaries. *Coast. Eng.* **2015**, *101*, 35–47. [CrossRef]
59. Willmott, C.J.; Ackleson, S.G.; Davis, R.E.; Feddema, J.J.; Klink, K.M.; Legates, D.R.; O'Donnell, J.; Rowe, C.M. Statistics for the evaluation and comparison of models. *J. Geophys. Res. Ocean.* **1985**, *90*, 8995–9005. [CrossRef]
60. Sogut, E. Wave and Current Interactions with Sharp-Edged Beachfront Structures on Rigid and Erodible Berms. Ph.D. Dissertation, State University of New York, Stony Brook, NY, USA, 2021.
61. Wilcox, D.C. Multiscale model for turbulent flows. *AIAA J.* **1988**, *26*, 1311–1320. [CrossRef]
62. Wilcox, D.C. *Turbulence Modeling for CFD*; DCW Industries: La Canada, CA, USA, 1998; Volume 2, pp. 103–217.
63. Wilcox, D.C. Formulation of the k-w turbulence model revisited. *AIAA J.* **2008**, *46*, 2823–2838. [CrossRef]
64. Harlow, F.H.; Nakayama, P.I. Turbulence transport equations. *Phys. Fluids* **1967**, *10*, 2323–2332. [CrossRef]
65. Rodi, W. *Turbulence Models and Their Application in Hydraulics*; CRC Press: London, UK, 2000.
66. Yakhot, V.; Orszag, S.A. Renormalization group analysis of turbulence. I. Basic theory. *J. Sci. Comput.* **1986**, *1*, 3–51. [CrossRef]
67. Yakhot, V.; Smith, L.M. The renormalization group, the ε-expansion and derivation of turbulence models. *J. Sci. Comput.* **1992**, *7*, 35–61. [CrossRef]
68. Menter, F.R. Elements of inductrial heat tranfer predictions. In Proceedings of the 16th Brazilian Congress of Mechanical Engineering (COBEM), Uberlandia, Brazil, 26–30 November 2001.
69. Menter, F.R.; Kuntz, M.; Langtry, R. Ten years of industrial experience with the SST turbulence model. *Turbul. Heat Mass Transf.* **2003**, *4*, 625–632.
70. Pope, S.B. Turbulent flows. *Meas. Sci. Technol.* **2001**, *12*, 2020–2021. [CrossRef]